Characterization of kHz Repetition Rate Laser-Driven Electron Beams by an Inhomogeneous Field Dipole Magnet Spectrometer

Illia Zymak [1,*], Marco Favetta [2,3,4,*], Gabriele Maria Grittani [1], Carlo Maria Lazzarini [1,5], Gianfranco Tassielli [6,7], Annika Grenfell [1], Leonardo Goncalves [1], Sebastian Lorenz [1,5], Vanda Sluková [1,5], Filip Vitha [1,5], Roberto Versaci [1], Edwin Chacon-Golcher [1], Michal Nevrkla [1,5], Jiří Šišma [1,5], Roman Antipenkov [1], Václav Šobr [1], Wojciech Szuba [1], Theresa Staufer [8], Florian Grüner [8], Loredana Lapadula [3], Ezio Ranieri [9], Michele Piombino [3], Nasr A. M. Hafz [10], Christos Kamperidis [10], Daniel Papp [10], Sudipta Mondal [10], Pavel Bakule [1] and Sergei V. Bulanov [1,11]

1. ELI Beamlines, The Extreme Light Infrastructure ERIC, Za Radnicí 835, 25241 Dolní Břežany, Czech Republic; gabriele.grittani@eli-beams.eu (G.M.G.); carlomaria.lazzarini@eli-beams.eu (C.M.L.); annika.grenfell@eli-beams.eu (A.G.); leonardo.vilanova@eli-beams.eu (L.G.); sebastian.lorenz@eli-beams.eu (S.L.); van.slukova@gmail.com (V.S.); filip.vitha@eli-beams.eu (F.V.); michal.nevrkla@eli-beams.eu (M.N.); jiri.sisma@eli-beams.eu (J.Š.); roman.antipenkov@eli-beams.eu (R.A.); vaclav.sobr@eli-beams.eu (V.Š.); wojciech.szuba@eli-beams.eu (W.S.); pavel.bakule@eli-beams.eu (P.B.); sergei.bulanov@eli-beams.eu (S.V.B.)
2. U.O.S.D. Fisica Sanitaria, Azienda Ospedaliero Universitaria Consorziale Policlinico, Piazza Giulio Cesare 11, 70124 Bari, Italy
3. U.O.S.D. Radioterapia, Azienda Ospedaliero Universitaria Consorziale Policlinico, Piazza Giulio Cesare 11, 70124 Bari, Italy; loredana.lapadula@policlinico.ba.it (L.L.); michele.piombino@policlinico.ba.it (M.P.)
4. U.O.S.D. Fisica Sanitaria e Radioterapia Trapani, Azienda Sanitaria Provinciale Trapani, Via Giuseppe Mazzini 1, 91100 Trapani, Italy
5. Faculty of Nuclear Sciences and Physical Engineering, Czech Technical University in Prague, Brehova 7, 11519 Prague, Czech Republic
6. Dipartimento di Medicina e Chirurgia, Università LUM "Giuseppe Degennaro", S.S. 100 Km. 18, Casamassima, 70010 Bari, Italy; tassielli@lum.it
7. Dipartimento Interateneo di Fisica "M. Merlin", Università degli Studi di Bari Aldo Moro, Via E. Orabona, 70125 Bari, Italy
8. Physics Department, and Center for Free-Electron Laser Science, University of Hamburg, Luruper Chaussee 149, 22761 Hamburg, Germany; theresa.staufer@uni-hamburg.de (T.S.); florian.gruener@uni-hamburg.de (F.G.)
9. Dipartimento di Bioscienze, Biotecnologie ed Ambiente, Università degli Studi di Bari Aldo Moro, Via E. Orabona, 70125 Bari, Italy; ezio.ranieri@uniba.it
10. The Extreme Light Infrastructure ERIC, ALPS Facility, ELI-HU Non-Profit Ltd., Wolfgang Sandner Utca 3, H-6728 Szeged, Hungary; nasr.hafiz@eli-alps.hu (N.A.M.H.); christos.kamperidis@eli-alps.hu (C.K.); daniel.papp@eli-alps.hu (D.P.); sudipta.mondal@eli-alps.hu (S.M.)
11. Kansai Photon Science Institute, National Institutes for Quantum and Radiological Science and Technology, Umemidai 8-1-7, Kizugawa 619-0215, Kyoto, Japan
* Correspondence: illia.zymak@eli-beams.eu (I.Z.); marco.favetta@asptrapani.it (M.F.)

Abstract: We demonstrate a method to characterize the beam energy, transverse profile, charge, and dose of a pulsed electron beam generated by a 1 kHz TW laser-plasma accelerator. The method is based on imaging with a scintillating screen in an inhomogeneous, orthogonal magnetic field produced by a wide-gap magnetic dipole. Numerical simulations were developed to reconstruct the electron beam parameters accurately. The method has been experimentally verified and calibrated using a medical LINAC. The energy measurement accuracy in the 6–20 MeV range is proven to be better than 10%. The radiation dose has been calibrated by a water-equivalent phantom, RW3, showing a linear response of the method within 2% in the 0.05–0.5 mGy/pulse range.

Keywords: laser wakefield acceleration; high repetition rate high power laser; electron beam metrology; phosphorous screen detector; Monte Carlo particle–matter interaction model; relativistic particle tracking model

1. Introduction

Electron accelerators are used in multiple fields, for example, in industry, medicine (for diagnostics and radiotherapy [1–4]), material science [5,6], particle physics research (to drive secondary photon production [7,8]), laboratory analog of space environment [9–11], and for research on Radiation Effects on Electronics (R2E) [12].

Conventional linear accelerators (LINAC) [13] or high-energy storage rings [14] based on radio-frequency (RF) technology are used to generate particle beams with energies in the MeV-to-TeV range. RF accelerators are a mature technology but are limited by acceleration gradients of around 100 MV/m before suffering from RF breakdown [15]. Laser-Plasma Acceleration (LPA) techniques [16–24] overcome this limitation and may increase the availability of relatively compact radiation sources for medical imaging [25,26], radiotherapy, AMO science [27–30], photon production (including material diagnostics applications [31–33]), R2E research and tests of CubeSat-dimensioned systems [34] (required for preflight approval). Since real-life applications require minimum current in the range from nA to μA, while the electron bunch charge is intrinsically limited to the pC-nC range for LPA [35], the use of high repetition rate laser systems (kHz) is required to raise the technology readiness level from a proof-of-concept status to an operational beamline [36–40], with the potential of reaching the beam parameters required for FLASH therapy [41,42].

An instance of an operational LPA-based electron beamline has been implemented at ELI. The ALFA (Allegra Laser For Acceleration) beamline is driven by a TW-class, 1 kHz, 15 fs L1-Allegra laser. This beamline can deliver electrons with energy in the tens of MeV [43]. To achieve this, previously developed LPA targets and beam diagnostic techniques [44–50] were integrated with a high repetition rate high-power laser.

An important challenge in the implementation of this beamline was the need to prevent the interaction of the high-power laser with any surface downstream from the LPA target until laser fluence would get below the damage threshold. To address this challenge, a compact Electron Beam Diagnostic System (EBDS) has been developed. EBDS provides reliable dose, energy, and beam transverse profile measurements. The system consists of a magnet coupled with other conventional components, such as a slit collimator, a scintillation screen, and a CMOS camera. To prevent intercepting the expanding laser beam and to allow for a wide electron beam acceptance angle, the device design is based on a wide-gap permanent magnetic dipole, where the pole distance is comparable to or larger than the magnet width and length [51,52]. The wide gap EBDS can also characterize ring-shaped beams [53–56]. A significant trade-off of such geometry is the loss of magnetic field homogeneity. The resulting beam deflection depends on the local magnetic field vector over the electron trajectory. In this case, the constant magnetic field approximation is not precise [57]. A comprehensive model based on the relativistic equations of motion for the electrons in the three-dimensional simulated magnetic field is required to accurately reconstruct the electron spectrum. The rest of this work describes the design of the EBDS, its integration with the 1 kHz ALFA beamline, the model for the spectrum reconstruction, and finally, the calibration methods for dose and charge, in which a reference LINAC was used.

2. Design of the EBDS

Numerical models (Section 2.1) were used to design the optimal geometry (i.e., slit depth, gap width) and to select the characteristics of various components needed for the reconstruction of the energy spectrum. These models also helped to estimate various operational parameters such as energy measurement range and maximum theoretical resolution. A conventional medical LINAC was used to verify the spectrum measurement method and perform a dose calibration of the scintillation screen and its imaging system (Section 3.1). The dose measurements are used to derive the beam charge using Monte Carlo simulations.

2.1. EBDS Setup for ALFA Beamline

The development of the EBDS setup comprised several stages: (a) selection of measurement techniques and components (Section 2.1.1); (b) modeling and verification of the magnetic field configuration and the corresponding calculation of the electron trajectories needed to infer the energy spectrum; (c) implementation of Monte Carlo models to estimate: (i) the effects of the electrons impinging on EBDS components, (ii) distribution of the electrons on the scintillator screen, and (iii) the dose on a water target for a given charge.

2.1.1. Design

The design of the EBDS was based on the constraints imposed by the ALFA beamline [43]. Basic technical requirements are firstly, measurement of electron energies up to 100 MeV (albeit at decreasing resolution at the higher energy values) and a wide acceptance angle; secondly, to avoid any laser-induced damage and vacuum contamination; thirdly, to satisfy the radioprotection, safety, and control requirements of the beamline.

The EBDS setup (Figure 1) consists of commercially available components except for an in-house assembled permanent magnetic dipole. The electron beam imaging system consists of a phosphorous LANEX Fast Back screen and a global shutter camera (Basler acA2040-25gm with CMOS sensor, 12-bit analog-to-digital converter, and a 16 mm/f1.6 objective). The screen has a charge density saturation level orders of magnitude higher [45] than the ones achievable in the ALFA beamline. The camera looks at the phosphorous screen through a flat mirror (Figure 1) since it must be placed off-axis to minimize radiation effects on the camera. Before the LANEX screen, a thin (up to 40 μm) aluminum foil is mounted to filter out the optical range plasma emissions and infrared laser light. The electron beam is deflected by an insertable C-shaped permanent magnet to measure the kinetic energy. The spectrometer has an electron beam acceptance angle of 210 mrad. To improve the resolution of the spectrometer, an insertable slit aperture of size 2 or 5 mm was used [51]. The distance from the slit to the laser focal spot is chosen to keep the laser intensity below the ablation threshold for fs lasers (0.6 J/cm^2 for aluminum) and to avoid material sputtering (more details in Section 2.1.3). The slit has a diffuse polish finish and is placed at a 2° angle to prevent laser back-reflection. The LANEX Fast Back emits approximately 90% of light within 1 ms after irradiation. This has to be taken into account for single pulse imaging when the exposure time of the camera is set to be 990 μs (the camera shutter jitter is below 1 μs).
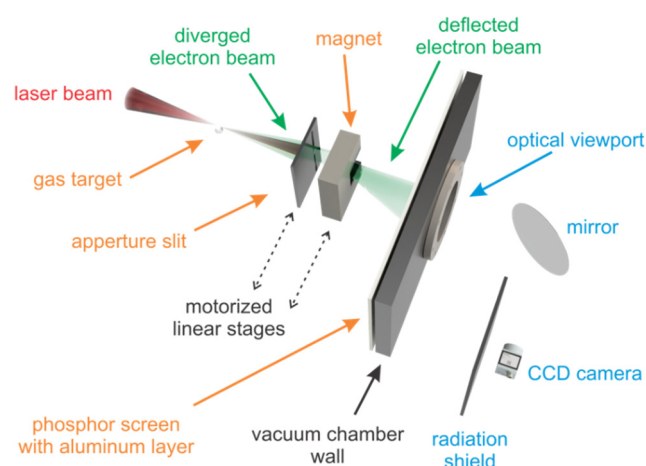
Figure 1. Top-view scheme of the EBDS system integrated into the ALFA accelerator. The components in vacuum and air are labeled with orange and blue colors, respectively.

The energy of the electrons is measured with respect to the farthermost edge of the aperture (opposite from the deflection direction), as described using simulation results in Sections 2.1.2 and 2.1.3. This procedure ensures a low estimate of the electron energy. The

electron beam spectrum reconstruction is performed similarly to the work described in [44]. It starts with the integration of the LANEX image values in the orthogonal dimension of the beam deflection. Then, each pixel is assigned a respective kinetic energy value using the pre-calculated displacement-to-energy conversion function for the specific beam pointing. Finally, to obtain the electron beam spectrum, each spectral bin value is normalized by its spectral width.

2.1.2. Magnetic Field Geometry and Particle Tracking Models

A precise three-dimensional (3D) model of the highly inhomogeneous magnetic vector field was calculated (Figure 2) using ESRF's Radia toolkit [58,59], which uses the boundary integral method. This map was experimentally verified using a Hall effect magnetometer at several points. Secondly, the vector field was used to numerically compute electron trajectories under multiple conditions, specifically for electrons with energies between 1 and 100 MeV at various initial values (position and direction) using the SIMION field and particle trajectory simulation software [60], Figure 3a. These calculations were used to estimate the displacement-to-energy conversion function and find the device's final design parameters.
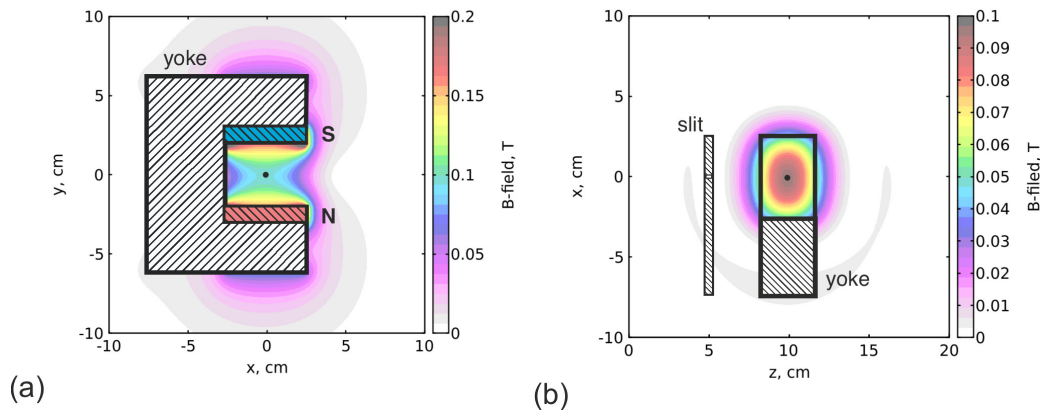
Figure 2. Map of the calculated magnetic field vector magnitude in planes crossing the center of the area between magnet poles indicated by the black dot: (**a**) plane orthogonal to the beam, (**b**) plane parallel to the beam. The distance between the magnet poles is 4 cm, and the length of the magnet is 4 cm.
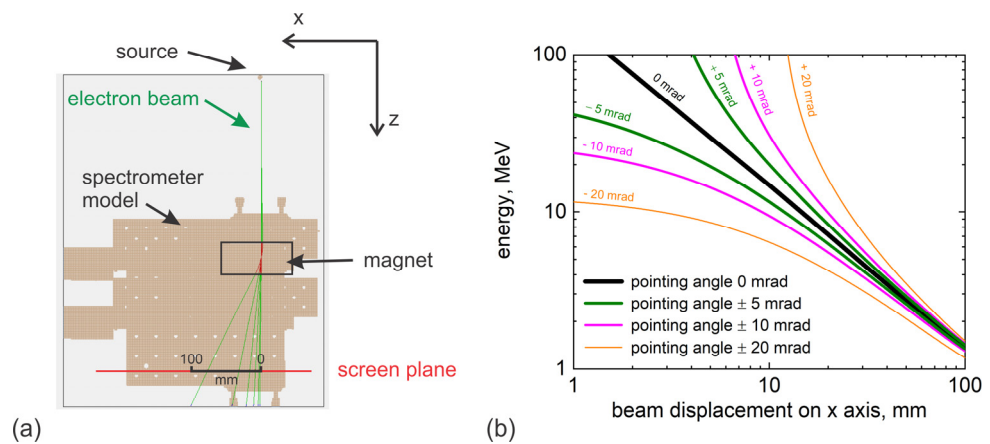
Figure 3. Theoretical electron beam trajectories calculated using the SIMION model: (**a**) for various energies in the range 1–100 MeV (electron trajectories out of the magnetic field are indicated in green, in the magnetic field in red); (**b**) beam displacement to energy for several beam pointing angles.

Thus, the use of the numerical model allows the generation of an individual calibration curve for specific vertical and horizontal beam-pointing values (Figure 3b). Maximal theoretical resolution and accuracy limits can be estimated for the experimental beam divergence and pointing (Figure 3b).

2.1.3. Monte Carlo Radiation Matter Interaction Simulations

The operation of the system depends on the interaction of relativistic particles with components of the EBDS, such as components of the energy spectrometer, electron beam detector, or irradiated phantom used for the calibration of the phosphorous screen. A Monte Carlo model has been developed to quantify these interactions, verify the geometry of the setup, and plan irradiation experiments (e.g., biological samples, detectors, and space-grade electronics).

FLUKA Monte Carlo simulations [61,62] have been used to study the electron beam propagation and its interaction with materials inside the ALFA setup (Figure 4) for the configuration of the setup with 16.6 cm target-to-slit, 3.9 cm slit-to-magnet, and 12.7 cm magnet-to-screen. This model is also used to estimate the beam profile contrast when the slit aperture is inserted. Simulations show an energy measurement resolution of $E/\Delta E = 2$ for 50 MeV and E/ΔE = 20 for 2 MeV. Beam scattering also reduces the spectrometer resolution at high energies. Energy measurement above 50 MeV requires pointing accuracy and divergence of a few mrad.
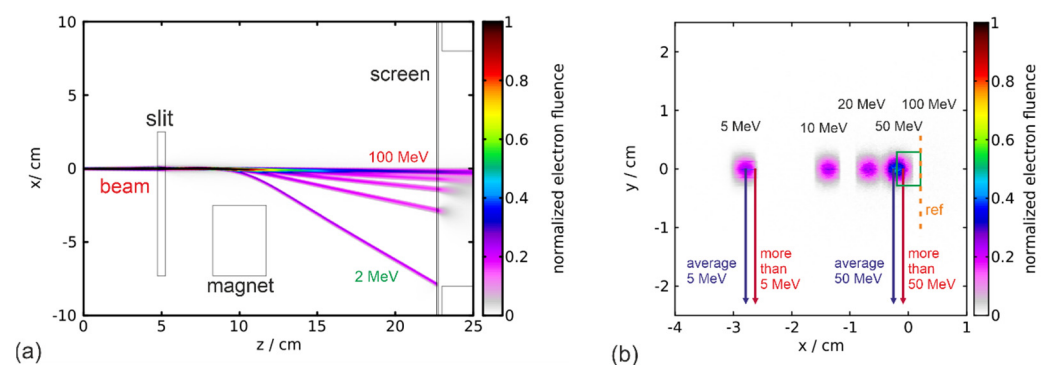

Figure 4. Electron fluence map calculated using FLUKA Monte Carlo simulation for 5 MeV, 10 MeV, 20 MeV, 50 MeV, and 100 MeV beams and a 2 mm slit aperture opening: (**a**) top view; (**b**) screen plane view. The model includes electron–matter interaction processes to evaluate resolution increasing with the aperture. Blue arrows indicate the average displacement of the beam, and red indicates the minimal possible displacement for the beam of a certain energy. Green rectangular allocates non-deflected beam. The orange "ref" line refers to the slit edge and indicates a reference to calculate minimal possible energy, and $x = 0$ coordinates the average energy for the measured deflection using the same calibration.

The FLUKA Monte Carlo model has also been used to evaluate the fluence from the EBDS dosimetry calibration. The absorbed-dose-to-fluence ratio depends on the energy of electrons and target properties (Figure 5). Dose deposition significantly depends on the geometry of the beam and target. The absorbed-dose-to-fluence ratio has been calculated by simulating the interaction of a 1 cm radius electron beam hitting a cylindrical water target (1 cm radius, 1 cm depth) [63]. It is constant in the 4–100 MeV energy range with an acceptable accuracy of a few percent. These results significantly differ from the thin target case shown in Figure 5 due to the scattering of primary electrons and the production of secondary particles during the beam propagation in the medium. The absorbed-dose-to-fluence ratio value of 560 ± 20 pC/cm^2/Gy slightly decreases for higher energies.
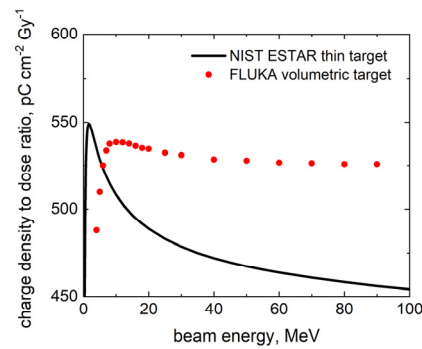
Figure 5. Theoretical dependence of the deposited dose to the beam charge density was calculated for a thin water layer using the NIST ESTAR database and for a 1 cm radius and 1 cm high water cylinder irradiated by the flattop profile beam of the same radius.

The developed FLUKA model was also used to optimize the geometry and energy distribution of the LPA-produced beam required for irradiation experiments to achieve more accurate dose delivery (Figure 6). The model allows the estimation of the effects of secondary particle generation in the EBDS, the beam profile shaping (using slits or beam focusing), and the analysis of beam focusing and profile distortion by a complete or partial insertion of the spectrometer magnet (Figure 6c). The partially inserted magnet option is important since it can be used for low-energy beam alignment with the output collimator, to pre-filter low-energy electrons, to improve control of the dose absorbed by the irradiated sample, and to characterize unwanted artifacts in EBDS. The experimentally measured profile of the beam deflected by the partially inserted magnet is shown in Section 3.2.
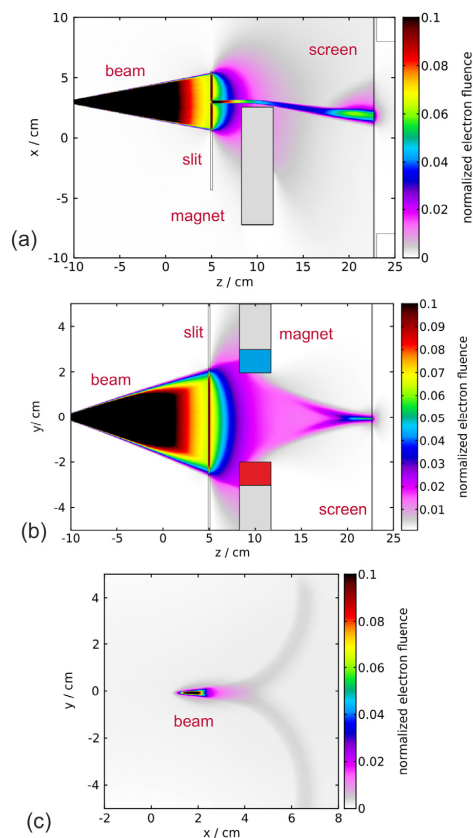

Figure 6. FLUKA model of the 300 mrad divergent 3 MeV electron beam propagating near the partially inserted magnet (30 mm offset), slit aperture is aligned with a beam: (**a**) top view; (**b**) side view; (**c**) screen plane view. The model is used to develop sample irradiation strategies and beam artifact analysis.

3. Results

The EBDS has been first verified and calibrated with a reference medical LINAC at the Policlinico di Bari (Section 3.1) and then commissioned in the LPA ALFA beamline at ELI (Section 3.2).

3.1. Calibration of the EDBS

Two separate experiments have been performed to verify the energy spectrum reconstruction and to calibrate the EBDS sensitivity to dose (and fluence).

Beam energy and fluence measurement have been verified and calibrated against the reference electron beams generated by the Elekta Synergy/Agility (Elekta Medical Systems, Crawley, UK) commercial medical LINAC, which has been comprehensively studied for accurate treatment planning [64,65]. The delivered dose is regularly verified in Policlinico di Bari (Italy) using the protocol standardized for medical applications [66]. To perform the calibration experiment at Policlinico di Bari, the EBDS has been transported to their radiation bunker and reassembled in the in-air area next to the output collimator of the LINAC, preserving the same geometry setup as it is used in ALFA.

Spectrometer calibration has been performed using LINAC beam energy as a reference. The calibration setup included, as for the ALFA configuration, the C-shaped magnet, phosphor screen, mirror, and a shielded CCD camera mounted off-axis, as shown in Figure 7a. The radiation shield made of polystyrene polymer material was used to decrease the camera background signal induced by R2E. The reference energy of the electron beam defined by the LINAC configuration was measured using the calculated beam displacement to energy dependence to validate the numerical model.
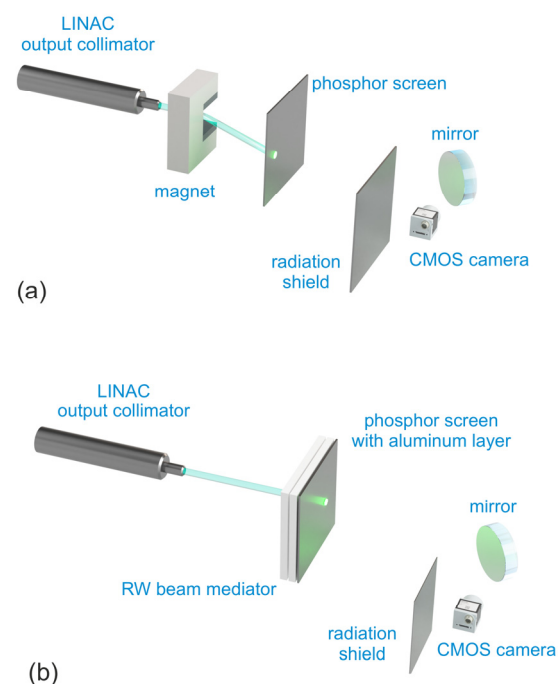
Figure 7. Experimental setup for the verification of the EBDS using the electron LINAC with, respectively, a 4 mm and 2 cm diameter round profile collimator as a reference source: (**a**) beam energy; (**b**) dose calibration. The magnet, Lanex screen, CMOS camera, mirror, and radiation shield are used as the electron detection system. The magnet or RW3 beam mediator slabs are inserted downstream from the screen for energy or dose calibration measurements.

The ratio of camera image intensity to dose (available for the solid water target equivalent) has been experimentally determined. The reference dose value has been measured using an Elekta beam circular collimator of diameter of 2 cm attached to the

LINAC head, solid water slabs (in RW3 polymer [67]), and a planar ionization chamber (Markus type, IBA PPC05 [68] interfaced with an electrometer IBA Dose 1).

The dose calibration was performed by placing the front surface of the water phantom at a source-to-target distance of 100 cm and by assembling the phantom as follows: an RW3 slab of a necessary thickness (1 cm or 2 cm, see Table 1), used as beam moderator, the ionization chamber placed immediately afterward inside a proper RW3 holder, and a stack of RW3 slabs with a total thickness of 5 cm. The beam energy (LINAC nominal energy) was varied from 6 MeV to 20 MeV, using all the available energy values in the range, see Table 1. A shot of the same beam intensity (100 MU, Monitor Unit of the LINAC system) for each energy was deposited to perform a single dose measurement. Each measurement was repeated 5 times to evaluate the average and standard deviation values. The average dose values are reported in Table 1.

Table 1. Reference dose deposition.

Nominal Beam Energy [MeV]	RW3 Slab Width [cm]	Absorbed Dose [Gy]	Dose Error [Gy]
4	1	0.260	0.008
6	1	0.45	0.01
8	1	0.60	0.02
10	1	0.72	0.02
10	2	0.60	0.02
12	2	0.74	0.02
15	2	0.88	0.03
18	2	1.02	0.03
20	2	1.07	0.03

The IBA PPC05 ionization chamber used was installed in conformity with the recommendations for the beam-to-chamber size ratio for small fields dosimetry set by the American Association of Physicists in Medicine (AAPM) [69]. This ensured high measurement accuracy. However, to preserve the EBDS geometry, the calibration setup was constructed at the limit of the AAPM recommended dimensions and did not satisfy the Bragg–Gray cavity conditions. Two studies [70,71] report that an error of about 2% on the dose measurement is obtained using a parallel plane ionization chamber like the one used in the present study. So, the total error in dose measurements is estimated at 3%, including the geometry factor and the tolerance of the used devices.

Afterward, the scintillating screen was placed instead of the PPC05 Ionization Chamber so its intensity could be measured with a beam that delivers a known dose. The experimental setup consisted of the same LANEX Fast Back phosphor screen with the aluminum layer, CCD camera, and optical system, as it is typically used for beam diagnostics (Figure 7b). The RW3 water equivalent polymer slab was used to absorb the beam energy and to modulate the dose downstream. The beam energy absorption is different for various electron energies, so the dose detected after the RW3 moderator by the screen and ionizing chamber has been changed by both the variation of the beam energy and the slab thickness.

The screen-to-camera optical path length was kept equal during calibration and during operation to maintain a constant camera collection angle.

To verify the EBDS performance, different reference energies provided by the medical LINAC in the range of 6 MeV to 20 MeV have been measured with the setup shown in Figure 7a. The electron beam profile has been shaped using a 4 mm diameter output electron collimator. Each energy spectrum measurement is averaged over at least 30 screen images to reduce camera noise.

The reference beam position without the deflection by the magnetic field has been determined from the position of the secondary photon beam spot. These secondary photons are generated in the collimator. The average energy of the beam over several LINAC shots

is defined as the center of mass of the energy distribution, retrieved from the numerical model used to correlate the displacement position with the energy values.

Figure 8 shows the linear agreement between measured and reference LINAC energies; this proves the reliability of the EBDS in measuring the electron energy spectra.
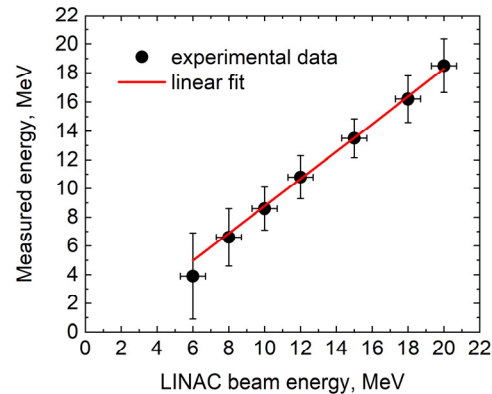

Figure 8. Verification of the beam energy measurement with the EBDS based on numerical models using a reference radiation source. Horizontal error bars are smaller than the markers. The linear fit is calculated using the least squares algorithm.

The systematic error between the measured and the reference energies was found to be lower than 10%. For energies above 8 MeV, the deviation from linear fit is less than 1%. Error bars of individual measurements (indicated in Figure 8) are determined as the width of the measured energy peak at half maximum (the statistical deviation is significantly lower than the peak width).

The decrease of the electron beam energy from the reference values is expected due to the scattering in the LINAC head and through the external collimators. The details of the scattering elements inside the LINAC head that can be used for the energy spread estimation are only approximately known from the vendor technical manual [72]. The international guideline IAEA-trs398 [67] gives a method to estimate the energy peak values in a standard configuration but not the energy spread. Energy peak fluctuation measured for standard conditions is about 0.5 MeV, and an estimation of the energy spread width [73,74] is about 1 MeV. The resulting error bar is estimated for the reference energy, which is about 0.7 MeV.

An ionization chamber dosimeter has been used to calibrate the EBDS reading of the electron beam dose and charge.

The calibration procedure consisted of relating the phosphor screen luminance (normalized to the camera sensor saturation level) to the reference dose value measured with the ionization chamber dosimeter. The results are shown in Figure 9.

The average dose deposited over the duration of each ionization chamber measurement (set to 15 s) is adjusted over the range of 0.2–1.1 Gy using various water-equivalent moderator slabs and by tuning the energy of the reference beam, as detailed in Table 1. For each measurement, the camera was acquired for 200 ms; therefore, the reference dose shown in Figure 9 has been adjusted to this time frame.

From the linear fit of the experimental data set, the resulting dose value to saturate the camera sensor is 34 ± 5 mGy. This corresponds (see Figure 5 for reference) to 16.6 ± 3 pC/cm^2 (or 3 fC per pixel) electron beam charge density accumulated over the camera exposure time.

These parameters can be used to estimate the sensitivity (absolute yield) of the screen to the electron radiation. The performed calibration of the phosphorous screen allows measurement of a delivered dose from a single shot to the integration of all shots used to deliver a required dose. This facilitates the measurement of values from a camera background level (<1 mGy) to hundreds of Gy integrated over an irradiation session.

Considering the optical system collecting angle of 0.6 msr and the screen-to-camera scale of 63 pixels per centimeter (see Section 2.1), the camera saturation level (19,000 photons

per pixel, according to specification [75] corresponds to a radiance of 1.6×10^{11} photons/sr/cm² on the EBDS screen. This is equivalent to a screen absolute yield of 9.6×10^9 photons/sr/pC.
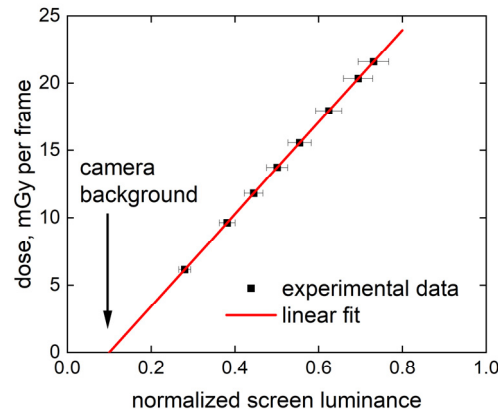

Figure 9. Calibration curve relating the phosphor screen luminance with the ionization chamber dose. Screen intensity, normalized to the camera luminance range, is calibrated over the water phantom absorbed dose value. The average measurement accuracy defined by the linear fit is better than 2%. Vertical error bars are smaller than the marker size.

3.2. Electron Beam Characterization in the ALFA Beamline

The EBDS has been then integrated and used to characterize the LPA electron beams produced with ALFA beamline [43]. Figures 10 and 11 show examples of electron beam and spectra reconstruction for the cases of nitrogen and a mixture of helium and nitrogen gas targets, respectively.
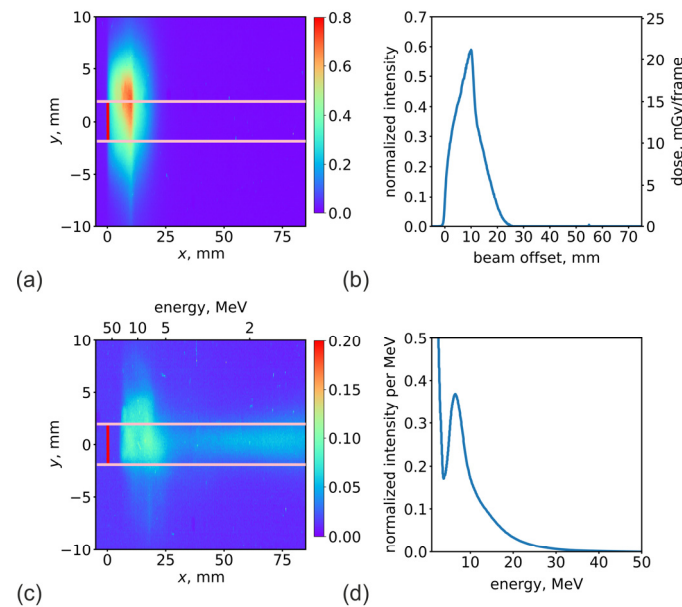
Figure 10. Reconstruction of the energy spectrum for the nitrogen gas target used in the ALFA beamline: (**a**) reference beam pointing image on the LANEX phosphor screen, without the magnet; (**b**) profile of the reference beam without the magnetic field, used to determine the absolute dose and the beam fluence; (**c**) deflected beam profile image; (**d**) energy spectrum obtained from the profile of the deflected beam with energy binning. The area between pink lines is used to assess the beam profile and reconstruct the spectrum. The red line indicates the reference beam pointing used for the spectrum reconstruction.

Figure 11. Evaluation of the energy spectrum for the gas mixture (98% Helium–2% Nitrogen) target: (**a**) profile of the beam deflected with the magnetic field; (**b**) evaluated spectrum with energy binning. The area between pink lines is used to assess the beam profile and reconstruct the spectrum. The red line indicates the reference beam pointing used for the spectrum reconstruction.
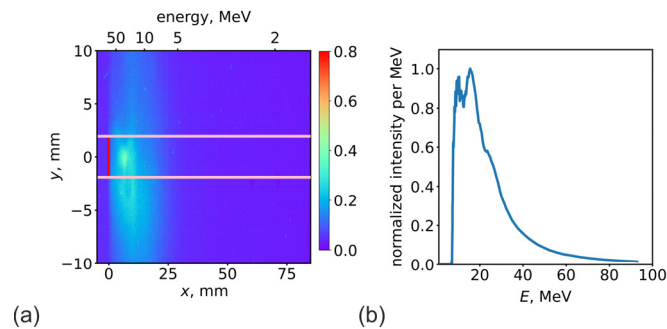
Compared to the medical LINAC, ALFA electron beams have a shot-to-shot pointing fluctuation. For this reason, the electron beam pointing must be defined as an average over several beams at fixed conditions. The beam profile, which Integrates over 10 electron bunches and spectrum measurements, is shown in Figure 10a–d, respectively. However, the energy spectrum can be measured for a single shot using a conservative reference pointing, taking the maximal possible displacement of the beam from the farthermost edge of the slit aperture. The energy spectrum measured from this displacement (marked in red in Figures 10 and 11) gives a lower estimate of the energy for a single bunch.

Finally, we observed experimentally the low energy focusing effect predicted by the simulation (Figure 6). In Figure 12, we show a focused 3 MeV beam. Moreover, by moving the magnet transversally, it was possible to steer the electron beam.
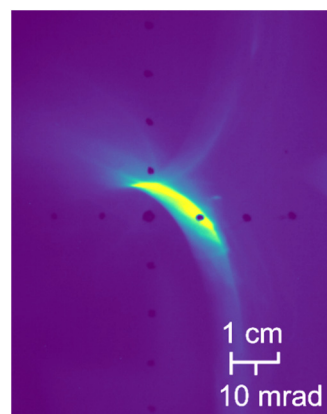

Figure 12. MeV-range electron beam profile obtained with the partially inserted slit and magnet technique integrated over 20 shots. This enhanced contrast color scale profile was generated with a nitrogen target. The dots indicate a 1 cm scale.

4. Summary

A compact electron spectrometer has been designed, developed, calibrated, and commissioned in the LPA ALFA beamline. The diagnostic setup has been optimized to work at high vacuum ($<10^{-6}$ mbar) in a 1 kHz high-intensity laser environment.

The setup's ability to measure energy and fluence has been calibrated at the Policlinico di Bari with a reference LINAC. The experimental results shown in the present work demonstrate the concept of a compact electron energy spectrometer for kHz LPA, with predictable measurement accuracy within its design parameters.

The design is based on a wide-gap permanent dipole magnet with an inhomogeneous magnetic field. The EBDS wide-gap dipole results in a 210 mrad acceptance angle, compared to the 380 mrad when the magnet is slid out (limited by LANEX screen size). The deflection

curve has been calculated by particle tracking in the numerically simulated inhomogeneous magnetic field.

The experimental energy calibration and verification demonstrate an accuracy of 10%. The measurement resolution, estimated using a numerical model, is E/DE = 2–20 over the 2–50 MeV range. The linearity of the measurement is found to be better than 1% in the 8–20 MeV range.

Beam transverse profile measurement is limited by the camera resolution (typically 6–8 pixels per 1 mm at the scintillation screen plane). The absolute yield measured in this work for the scintillation LANEX Fast Back screen (9.6×10^9 photons/sr/pC) is 30% higher than LANEX Regular [45]. Our calibration assumes the same response of the LANEX Fast Back screen to the LINAC and LPA electron beams, which have different time structures.

This method is of fundamental importance for irradiation applications such as biomedical and R2E research, as it allows for control over the irradiation process and dose delivery to the sample in the mGy to kGy range.

Author Contributions: Writing—original draft preparation, methodology, software, visualization, I.Z.; writing—review and editing, methodology, formal analysis, M.F., G.M.G., E.C.-G. and C.M.L.; methodology, L.G., S.L., V.S., F.V., A.G., R.V., M.N., J.Š., R.A., V.Š., W.S., T.S., F.G., L.L., G.T., E.R., M.P., N.A.M.H., C.K., D.P., S.M. and P.B.; project administration G.M.G.; supervision, funding acquisition, S.V.B. All authors have read and agreed to the published version of the manuscript.

Institutional Review Board Statement: Not applicable.

Informed Consent Statement: Not applicable.

Data Availability Statement: The raw data supporting the conclusions of this article will be made available by the authors on request.

Conflicts of Interest: The authors declare no conflicts of interest. The funders had no role in the design of the study; in the collection, analyses, or interpretation of data; in the writing of the manuscript; or in the decision to publish the results.

References

1. Citrin, D.E. Recent Developments in Radiotherapy. *N. Engl. J. Med.* **2017**, *377*, 1065–1075. [CrossRef] [PubMed]
2. Hogstrom, K.R.; Almond, P.R. Review of Electron Beam Therapy Physics. *Phys. Med. Biol.* **2006**, *51*, R455. [CrossRef]
3. Zurrida, S.; Veronesi, U. Milestones in Breast Cancer Treatment. *Breast J.* **2015**, *21*, 3–12. [CrossRef]
4. Chancellor, J.C.; Scott, G.B.I.; Sutton, J.P. Space Radiation: The Number One Risk to Astronaut Health beyond Low Earth Orbit. *Life* **2014**, *4*, 491–510. [CrossRef]
5. Henniges, U.; Hasani, M.; Potthast, A.; Westman, G.; Rosenau, T. Electron Beam Irradiation of Cellulosic Materials—Opportunities and Limitations. *Materials* **2013**, *6*, 1584–1598. [CrossRef] [PubMed]
6. Harrysson, O.L.A.; Cansizoglu, O.; Marcellin-Little, D.J.; Cormier, D.R.; West, H.A. Direct Metal Fabrication of Titanium Implants with Tailored Materials and Mechanical Properties Using Electron Beam Melting Technology. *Mater. Sci. Eng. C* **2008**, *28*, 366–373. [CrossRef]
7. Michel, P. The Radiation Source ELBE at the Forschungszentrum Dresden-Rossendorf. In Proceedings of the 2008 IEEE Nuclear Science Symposium Conference Record, Dresden, Germany, 19–25 October 2008; pp. 3078–3080.
8. Sampath, A.; Davoine, X.; Corde, S.; Gremillet, L.; Gilljohann, M.; Sangal, M.; Keitel, C.H.; Ariniello, R.; Cary, J.; Ekerfelt, H.; et al. Extremely Dense Gamma-Ray Pulses in Electron Beam-Multifoil Collisions. *Phys. Rev. Lett.* **2021**, *126*, 64801. [CrossRef]
9. Li, W.; Hudson, M.K. Earth's Van Allen Radiation Belts: From Discovery to the Van Allen Probes Era. *J. Geophys. Res. Space Phys.* **2019**, *124*, 8319–8351. [CrossRef]
10. Zymak, I.; Antipenkov, R.; Favetta, M.; Grittani, G.; Grenfell, A.; Lazzarini, C.M.; Goncalves, L.; Sobr, V.; Špaèek, A.; Szuba, W.; et al. Electron Beam Characterization and First Experimental Results for the Laser Wake Field Accelerator for Radiation to Electronics Effects Applications. In Proceedings of the 2022 22nd European Conference on Radiation and Its Effects on Components and Systems (RADECS), Venice, Italy, 3–7 October 2022.

11. Zymak, I.; Antipenkov, R.; Gonçalves, L.; Grittani, G.; Lazzarini, C.M.; Lorenz, S.; Nevrkla, M.; Versaci, R.; Bakule, P.; Bulanov, S.V. Conceptual Design of a Novel Electron Radiation and Spacecraft Charging Test Platform for CubeSat Dimensioned Devices Based on Laser-Driven Electron Accelerator. In Proceedings of the 2021 21th European Conference on Radiation and Its Effects on Components and Systems (RADECS), Vienna, Austria, 13–17 September 2021; pp. 1–4.

12. Olifer, L.; Mann, I.R.; Claudepierre, S.G.; Baker, D.N.; Spence, H.E.; Ozeke, L.G. A Natural Limit to the Spectral Hardness of Worst Case Electron Radiation in the Terrestrial Van Allen Belt. *J. Geophys. Res. Space Phys.* **2022**, *127*, e2022JA030506. [CrossRef]

13. Martins, M.N.; Silva, T.F. Electron Accelerators: History, Applications, and Perspectives. *Radiat. Phys. Chem.* **2014**, *95*, 78–85. [CrossRef]

14. Tavares, P.F.; Leemann, S.C.; Sjöström, M.; Andersson, Å. The MAXIV Storage Ring Project. *J. Synchrotron Radiat.* **2014**, *21*, 862–877. [CrossRef]

15. Kovermann, J.W. Comparative Studies of High-Gradient Rf and Dc Breakdowns. Ph.D. Thesis, RWTH Aachen University, Aachen, Germany, 2010.

16. Hubbard, R.F.; Sprangle, P.; Hafizi, B. Scaling of Accelerating Gradients and Dephasing Effects in Channel-Guided Laser Wakefield Accelerators. *IEEE Trans. Plasma Sci.* **2000**, *28*, 1122–1132. [CrossRef]

17. Tajima, T.; Dawson, J.M. Laser Electron Accelerator. *Phys. Rev. Lett.* **1979**, *43*, 267–270. [CrossRef]

18. Maier, A.R.; Delbos, N.M.; Eichner, T.; Hübner, L.; Jalas, S.; Jeppe, L.; Jolly, S.W.; Kirchen, M.; Leroux, V.; Messner, P.; et al. Decoding Sources of Energy Variability in a Laser-Plasma Accelerator. *Phys. Rev. X* **2020**, *10*, 31039. [CrossRef]

19. Miao, B.; Shrock, J.E.; Feder, L.; Hollinger, R.C.; Morrison, J.; Nedbailo, R.; Picksley, A.; Song, H.; Wang, S.; Rocca, J.J.; et al. Multi-GeV Electron Bunches from an All-Optical Laser Wakefield Accelerator. *Phys. Rev. X* **2022**, *12*, 31038. [CrossRef]

20. Aniculaesei, C.; Ha, T.; Yoffe, S.; Labun, L.; Milton, S.; McCary, E.; Spinks, M.M.; Quevedo, H.J.; Labun, O.Z.; Sain, R.; et al. The Acceleration of a High-Charge Electron Bunch to 10 GeV in a 10-Cm Nanoparticle-Assisted Wakefield Accelerator. *Matter Radiat. Extrem.* **2023**, *9*, 014001. [CrossRef]

21. Geddes, C.G.R.; Toth, C.; van Tilborg, J.; Esarey, E.; Schroeder, C.B.; Bruhwiler, D.; Nieter, C.; Cary, J.; Leemans, W.P. High-Quality Electron Beams from a Laser Wakefield Accelerator Using Plasma-Channel Guiding. *Nature* **2004**, *431*, 538–541. [CrossRef] [PubMed]

22. Mangles, S.P.D.; Murphy, C.D.; Najmudin, Z.; Thomas, A.G.R.; Collier, J.L.; Dangor, A.E.; Divall, E.J.; Foster, P.S.; Gallacher, J.G.; Hooker, C.J.; et al. Monoenergetic Beams of Relativistic Electrons from Intense Laser–Plasma Interactions. *Nature* **2004**, *431*, 535–538. [CrossRef] [PubMed]

23. Faure, J.; Glinec, Y.; Pukhov, A.; Kiselev, S.; Gordienko, S.; Lefebvre, E.; Rousseau, J.-P.; Burgy, F.; Malka, V. A Laser–Plasma Accelerator Producing Monoenergetic Electron Beams. *Nature* **2004**, *431*, 541–544. [CrossRef] [PubMed]

24. Shrock, J.E.; Rockafellow, E.; Miao, B.; Le, M.; Hollinger, R.C.; Wang, S.; Gonsalves, A.J.; Picksley, A.; Rocca, J.J.; Milchberg, H.M. Guided Mode Evolution and Ionization Injection in Meter-Scale Multi-GeV Laser Wakefield Accelerators. *Phys. Rev. Lett.* **2024**, *133*, 45002. [CrossRef]

25. Brümmer, T.; Debus, A.; Pausch, R.; Osterhoff, J.; Grüner, F. Design Study for a Compact Laser-Driven Source for Medical x-Ray Fluorescence Imaging. *Phys. Rev. Accel. Beams* **2020**, *23*, 31601. [CrossRef]

26. Khrennikov, K.; Wenz, J.; Buck, A.; Xu, J.; Heigoldt, M.; Veisz, L.; Karsch, S. Tunable All-Optical Quasimonochromatic Thomson X-Ray Source in the Nonlinear Regime. *Phys. Rev. Lett.* **2015**, *114*, 195003. [CrossRef] [PubMed]

27. Wang, W.; Feng, K.; Ke, L.; Yu, C.; Xu, Y.; Qi, R.; Chen, Y.; Qin, Z.; Zhang, Z.; Fang, M.; et al. Free-Electron Lasing at 27 Nanometres Based on a Laser Wakefield Accelerator. *Nature* **2021**, *595*, 516–520. [CrossRef] [PubMed]

28. Labat, M.; Cabadağ, J.C.; Ghaith, A.; Irman, A.; Berlioux, A.; Berteaud, P.; Blache, F.; Bock, S.; Bouvet, F.; Briquez, F.; et al. Seeded Free-Electron Laser Driven by a Compact Laser Plasma Accelerator. *Nat. Photonics* **2023**, *17*, 150–156. [CrossRef]

29. Pompili, R.; Alesini, D.; Anania, M.P.; Arjmand, S.; Behtouei, M.; Bellaveglia, M.; Biagioni, A.; Buonomo, B.; Cardelli, F.; Carpanese, M.; et al. Free-Electron Lasing with Compact Beam-Driven Plasma Wakefield Accelerator. *Nature* **2022**, *605*, 659–662. [CrossRef]

30. Feldhaus, J.; Krikunova, M.; Meyer, M.; Möller, T.; Moshammer, R.; Rudenko, A.; Tschentscher, T.; Ullrich, J. AMO Science at the FLASH and European XFEL Free-Electron Laser Facilities. *J. Phys. B At. Mol. Opt. Phys.* **2013**, *46*, 164002. [CrossRef]

31. Zymaková, A.; Precek, M.; Picchiotti, A.; Błachucki, W.; Zymak, I.; Szlachetko, J.; Vankó, G.; Németh, Z.; Sá, J.; Wiste, T.; et al. X-Ray Spectroscopy Station for Sample Characterization at ELI Beamlines. *Sci. Rep.* **2023**, *13*, 17258. [CrossRef]

32. Corde, S.; Ta Phuoc, K.; Lambert, G.; Fitour, R.; Malka, V.; Rousse, A.; Beck, A.; Lefebvre, E. Femtosecond x Rays from Laser-Plasma Accelerators. *Rev. Mod. Phys.* **2013**, *85*, 1–48. [CrossRef]

33. Döpp, A.; Mahieu, B.; Lifschitz, A.; Thaury, C.; Doche, A.; Guillaume, E.; Grittani, G.; Lundh, O.; Hansson, M.; Gautier, J.; et al. Stable Femtosecond X-Rays with Tunable Polarization from a Laser-Driven Accelerator. *Light Sci. Appl.* **2017**, *6*, e17086. [CrossRef]

34. Zymak, I.; Žabka, J.; Polášek, M.; Sanderink, A.; Lebreton, J.-P.; Gaubicher, B.; Cherville, B.; Zymaková, A.; Briois, C. A High-Resolution Mass Spectrometer for the Experimental Study of the Gas Composition in Planetary Environments: First Laboratory Results. *Aerospace* **2023**, *10*, 522. [CrossRef]

35. Lu, W.; Tzoufras, M.; Joshi, C.; Tsung, F.S.; Mori, W.B.; Vieira, J.; Fonseca, R.A.; Silva, L.O. Generating Multi-GeV Electron Bunches Using Single Stage Laser Wakefield Acceleration in a 3D Nonlinear Regime. *Phys. Rev. Spec. Top.-Accel. Beams* **2007**, *10*, 61301. [CrossRef]

36. He, Z.-H.; Hou, B.; Nees, J.A.; Easter, J.H.; Faure, J.; Krushelnick, K.; Thomas, A.G.R. High Repetition-Rate Wakefield Electron Source Generated by Few-Millijoule, 30 Fs Laser Pulses on a Density Downramp. *New J. Phys.* **2013**, *15*, 53016. [CrossRef]

37. Guénot, D.; Gustas, D.; Vernier, A.; Beaurepaire, B.; Böhle, F.; Bocoum, M.; Lozano, M.; Jullien, A.; Lopez-Martens, R.; Lifschitz, A.; et al. Relativistic Electron Beams Driven by KHz Single-Cycle Light Pulses. *Nat. Photonics* **2017**, *11*, 293–296. [CrossRef]

38. Valenta, P.; Esirkepov, T.Z.; Koga, J.K.; Nečas, A.; Grittani, G.M.; Lazzarini, C.M.; Klimo, O.; Korn, G.; Bulanov, S. V Polarity Reversal of Wakefields Driven by Ultrashort Pulse Laser. *Phys. Rev. E* **2020**, *102*, 53216. [CrossRef]

39. Lazzarini, C.M.; Goncalves, L.V.; Grittani, G.M.; Lorenz, S.; Nevrkla, M.; Valenta, P.; Levato, T.; Bulanov, S.V.; Korn, G. Electron Acceleration at ELI-Beamlines: Towards High-Energy and High-Repetition Rate Accelerators. *Int. J. Mod. Phys. A* **2019**, *34*, 1943010. [CrossRef]

40. Salehi, F.; Le, M.; Railing, L.; Kolesik, M.; Milchberg, H.M. Laser-Accelerated, Low-Divergence 15-MeV Quasimonoenergetic Electron Bunches at 1 KHz. *Phys. Rev. X* **2021**, *11*, 21055. [CrossRef]

41. Cavallone, M.; Rovige, L.; Huijts, J.; Bayart, É.; Delorme, R.; Vernier, A.; Jorge, P.G.; Moeckli, R.; Deutsch, E.; Faure, J.; et al. Dosimetric Characterisation and Application to Radiation Biology of a KHz Laser-Driven Electron Beam. *Appl. Phys. B* **2021**, *127*, 57. [CrossRef]

42. Schulte, R.; Johnstone, C.; Boucher, S.; Esarey, E.; Geddes, C.G.R.; Kravchenko, M.; Kutsaev, S.; Loo, B.W.; Méot, F.; Mustapha, B.; et al. Transformative Technology for FLASH Radiation Therapy. *Appl. Sci.* **2023**, *13*, 5021. [CrossRef] [PubMed]

43. Lazzarini, C.M.; Grittani, G.M.; Valenta, P.; Zymak, I.; Antipenkov, R.; Chaulagain, U.; Goncalves, L.V.N.; Grenfell, A.; Lamač, M.; Lorenz, S.; et al. Ultrarelativistic Electron Beams Accelerated by Terawatt Scalable KHz Laser. *Phys. Plasmas* **2024**, *31*, 030703. [CrossRef]

44. Glinec, Y.; Faure, J.; Guemnie-Tafo, A.; Malka, V.; Monard, H.; Larbre, J.P.; De Waele, V.; Marignier, J.L.; Mostafavi, M. Absolute Calibration for a Broad Range Single Shot Electron Spectrometer. *Rev. Sci. Instrum.* **2006**, *77*, 103301. [CrossRef]

45. Buck, A.; Zeil, K.; Popp, A.; Schmid, K.; Jochmann, A.; Kraft, S.D.; Hidding, B.; Kudyakov, T.; Sears, C.M.S.; Veisz, L.; et al. Absolute Charge Calibration of Scintillating Screens for Relativistic Electron Detection. *Rev. Sci. Instrum.* **2010**, *81*, 033301. [CrossRef] [PubMed]

46. Lorenz, S.; Grittani, G.M.; Kondo, K.; Kon, A.; Liu, Y.-K.; Sagisaka, A.; Ogura, K.; Nakanii, N.; Huang, K.; Bierwage, A.; et al. In-Vacuum Post-Compression of Optical Probe Pulses for Relativistic Plasma Diagnostics. *High Power Laser Sci. Eng.* **2024**, *12*, e53. [CrossRef]

47. Vishnyakov, E.A.; Sagisaka, A.; Ogura, K.; Esirkepov, T.Z.; Gonzalez-Izquierdo, B.; Armstrong, C.D.; Pikuz, T.A.; Pikuz, S.A.; Yan, W.; Jeong, T.M.; et al. Metrology for Sub-Rayleigh-Length Target Positioning in ~1022 W/Cm^2 Laser–Plasma Experiments. *High Power Laser Sci. Eng.* **2024**, *12*, e32. [CrossRef]

48. Lorenz, S.; Grittani, G.; Goncalves, L.V.N.; Lazzarini, C.M.; Limpouch, J.; Nevrkla, M.; Bulanov, S.; Korn, G. Tomographic Reconstruction Algorithms for Structured Gas Density Profiles of the Targets for Laser Wakefield Acceleration. *Meas. Sci. Technol.* **2020**, *31*, 085205. [CrossRef]

49. Lorenz, S.; Grittani, G.M.; Chacon-Golcher, E.; Lazzarini, C.M.; Limpouch, J.; Nawaz, F.; Nevrkla, M.; Vilanova, L.; Levato, T. Characterization of Supersonic and Subsonic Gas Targets for Laser Wakefield Electron Acceleration Experiments. *Matter Radiat. Extrem.* **2019**, *4*, 015401. [CrossRef]

50. Downer, M.C.; Zgadzaj, R.; Debus, A.; Schramm, U.; Kaluza, M.C. Diagnostics for Plasma-Based Electron Accelerators. *Rev. Mod. Phys.* **2018**, *90*, 35002. [CrossRef]

51. Cha, H.J.; Choi, I.W.; Kim, H.T.; Kim, I.J.; Nam, K.H.; Jeong, T.M.; Lee, J. Absolute Energy Calibration for Relativistic Electron Beams with Pointing Instability from a Laser-Plasma Accelerator. *Rev. Sci. Instrum.* **2012**, *83*, 63301. [CrossRef]

52. Costa, G.; Anania, M.P.; Bisesto, F.; Chiadroni, E.; Cianchi, A.; Curcio, A.; Ferrario, M.; Filippi, F.; Marocchino, A.; Mira, F.; et al. Characterization of Self-Injected Electron Beams from LWFA Experiments at SPARC_LAB. *Nucl. Instrum. Methods Phys. Res. A* **2018**, *909*, 118–122. [CrossRef]

53. Russell, B.K.; Campbell, P.T.; Qian, Q.; Cardarelli, J.A.; Bulanov, S.S.; Bulanov, S.V.; Grittani, G.M.; Seipt, D.; Willingale, L.; Thomas, A.G.R. Ultrafast Relativistic Electron Probing of Extreme Magnetic Fields. *Phys. Plasmas* **2023**, *30*, 093105. [CrossRef]

54. Valenta, P.; Grittani, G.M.; Lazzarini, C.M.; Klimo, O.; Bulanov, S. V On the Electromagnetic-Electron Rings Originating from the Interaction of High-Power Short-Pulse Laser and Underdense Plasma. *Phys. Plasmas* **2021**, *28*, 122104. [CrossRef]

55. Kaganovich, D.; Gordon, D.F.; Ting, A. Observation of Large-Angle Quasimonoenergetic Electrons from a Laser Wakefield. *Phys. Rev. Lett.* **2008**, *100*, 215002. [CrossRef] [PubMed]

56. Pollock, B.B.; Tsung, F.S.; Albert, F.; Shaw, J.L.; Clayton, C.E.; Davidson, A.; Lemos, N.; Marsh, K.A.; Pak, A.; Ralph, J.E.; et al. Formation of Ultrarelativistic Electron Rings from a Laser-Wakefield Accelerator. *Phys. Rev. Lett.* **2015**, *115*, 55004. [CrossRef] [PubMed]

57. Nakamura, K.; Wan, W.; Ybarrolaza, N.; Syversrud, D.; Wallig, J.; Leemans, W.P. Broadband Single-Shot Electron Spectrometer for GeV-Class Laser-Plasma-Based Accelerators. *Rev. Sci. Instrum.* **2008**, *79*, 053301. [CrossRef]

58. Chubar, O.; Elleaume, P.; Chavanne, J. A Three-Dimensional Magnetostatics Computer Code for Insertion Devices. *J. Synchrotron Radiat.* **1998**, *5*, 481–484. [CrossRef] [PubMed]

59. Elleaume, P.; Chubar, O.; Chavanne, J. Computing 3D Magnetic Field from Insertion Devices. In Proceedings of the 1997 Particle Accelerator Conference (Cat. No.97CH36167), Vancouver, BC, Canada, 16 May 1997; pp. 3509–3511.

60. Dahl, D.A. SIMION for the Personal Computer in Reflection. *Int. J. Mass. Spectrom.* **2000**, *200*, 3–25. [CrossRef]

61. Battistoni, G.; Boehlen, T.; Cerutti, F.; Chin, P.W.; Esposito, L.S.; Fassò, A.; Ferrari, A.; Lechner, A.; Empl, A.; Mairani, A.; et al. Overview of the FLUKA Code. *Ann. Nucl. Energy* **2015**, *82*, 10–18. [CrossRef]

62. Ahdida, C.; Bozzato, D.; Calzolari, D.; Cerutti, F.; Charitonidis, N.; Cimmino, A.; Coronetti, A.; D'Alessandro, G.L.; Donadon Servelle, A.; Esposito, L.S.; et al. New Capabilities of the FLUKA Multi-Purpose Code. *Front. Phys.* **2022**, *9*, 788253. [CrossRef]

63. Horváth, D.; Grittani, G.; Precek, M.; Versaci, R.; Bulanov, S.V.; Olšovcová, V. Time Dynamics of the Dose Deposited by Relativistic Ultra-Short Electron Beams. *Phys. Med. Biol.* **2023**, *68*, 22NT01. [CrossRef]

64. Chojnowski, J.M.; Taylor, L.M.; Sykes, J.R.; Thwaites, D.I. Beam Focal Spot Position Determination for an Elekta Linac with the Agility® Head; Practical Guide with a Ready-to-Go Procedure. *J. Appl. Clin. Med. Phys.* **2018**, *19*, 44–47. [CrossRef] [PubMed]

65. Van Eeden, D.; Sachse, K.N.; du Plessis, F.C.P. Validation of a Lévy Electron Energy Straggling Model for an Elekta Synergy® Linear Accelerator. *Appl. Radiat. Isot.* **2020**, *164*, 109244. [CrossRef] [PubMed]

66. Andreo, P.; Burns, D.T.; Hohlfeld, K.; Huq, M.S.; Kanai, T.; Laitano, F.; Smythe, V.G.; Vynckier, S. *; Absorbed Dose Determination in External Beam Radiotherapy: An International Code of Practice for Dosimetry Based on Standards of Absorbed Dose to Water*; Technical Reports Series No. 398; International Atomic Energy Agency (IAEA): Vienna, Austria, 2000; ISBN 0074-1914.

67. Water-Equivalent RW3 Slab Phantom with Chamber Adaptation Plates for Therapy Dosimetry. Available online: https://www.ptwdosimetry.com/en/products/rw3-slab-phantom (accessed on 15 August 2024).

68. PPC05 Plane Parallel Chamber for Absolute and Relative Electron Beam Dosimetry. Available online: https://www.iba-dosimetry.com/product/ppc05-plane-parallel-chamber (accessed on 15 August 2024).

69. Benedict, S.H.; Yenice, K.M.; Followill, D.; Galvin, J.M.; Hinson, W.; Kavanagh, B.; Keall, P.; Lovelock, M.; Meeks, S.; Papiez, L.; et al. Stereotactic Body Radiation Therapy: The Report of AAPM Task Group 101. *Med. Phys.* **2010**, *37*, 4078–4101. [CrossRef] [PubMed]

70. Saidani, I.; Salem, L.B.; Besbes, M. 34A Small Field Dosimetry for Electron Beams Using Four Types of Detectors. *Phys. Medica* **2018**, *56*, 55. [CrossRef]

71. Bayatiani, M.R.; Aliasgharzadeh, A.; Seif, F.; Mohaghegh, F.; Fallahi, F. Comparison of Dosimetric Parameters of Small-Field Electron Beams between Advanced Markus, Semiflex 3D, and Diode E Responses. *Radiol. Phys. Technol.* **2020**, *13*, 296–305. [CrossRef] [PubMed]

72. *Instruction for Use—Technical Reference Manual*; Elekta: Stockholm, Sweden, 2011.

73. Apaza Veliz, D.G.; Wilches Visbal, J.H.; Abrego, F.C.; Vega Ramírez, J.L. Monte Carlo Calculation of the Energy Spectrum of a 6 MeV Electron Beam Using PENetration and Energy Loss of Positrons and Electrons Code. *J. Med. Phys.* **2020**, *45*, 116–122. [CrossRef] [PubMed]

74. Rezzoug, M.; Zerfaoui, M.; Oulhouq, Y.; Rrhioua, A. Using PRIMO to Determine the Initial Beam Parameters of Elekta Synergy Linac for Electron Beam Energies of 6, 9, 12, and 15 MeV. *Rep. Pract. Oncol. Radiother.* **2023**, *28*, 592–600. [CrossRef] [PubMed]

75. Basler Ace AcA2040-25gm—EMVA Data. Available online: https://www2.baslerweb.com/en/downloads/document-downloads/basler-ace-aca2040-25gm-emva-data/?_gl=1*1nkbzpj*_up*MQ..&gclid=EAIaIQobChMIrpycjsP2hwMVI59oCR2TOgmoEAAYAiAAEgLUNPD_BwE (accessed on 15 August 2024).